10/12/20

1 Types of lightning discharges and lightning terminology

Lightning can be defined as a transient, high-current (typically tens of kiloamperes) electric discharge in air whose length is measured in kilometers. As for any discharge in air, the lightning channel is composed of ionized gas – that is, of plasma – whose peak temperature is typically 30,000 K—about five times higher than the temperature of the surface of the Sun. Lightning was present on Earth long before human life evolved, and it may even have played a crucial role in the evolution of life on our planet. The global lightning flash rate is some tens per second to 100 per second. Each year, some 25 million cloud-to-ground lightning discharges occur in the United States, and this number is expected to increase by about 50 percent due to global warming over the twenty-first century (Romps et al., 2014). Lightning initiates many forest fires, and over 30 percent of all electric power line failures are lightning related. Each commercial aircraft is struck by lightning on average once a year. A lightning strike to an unprotected object or system can be catastrophic.

1.1 Overview

(cloud-to-cloud)

The lightning discharge in its entirety, whether it strikes the ground or not, is usually termed a "lightning flash" or just a "flash." A lightning discharge that involves an object on the ground or in the atmosphere is referred to as a "lightning strike." A commonly used non-technical term for a lightning discharge is a "lightning bolt." About three quarters of lightning discharges do not involve the ground. They include intracloud, intercloud, and cloud-to-air discharges and are collectively referred to as cloud flashes (see Fig. 1.1) and sometimes as ICs. Lightning discharges between cloud and earth are termed cloud-to-ground (or just ground) discharges and sometimes referred to as CGs. The latter constitute about 25 percent of global lightning activity. About 90 percent or more of global cloud-to-ground lightning is accounted for by negative downward lightning, in which negative charge is effectively transported to the ground, and the initial process begins in the cloud and develops in the downward direction. The term "effectively" is used to indicate that individual charges are not transported all the way from the cloud to the ground during the lightning processes; rather, the flow of electrons (the primary charge carriers) in one part of the lightning channel results in the flow of other electrons in other parts of the channel. Other types of cloud-to-ground lightning include positive downward, negative upward, and positive upward discharges (see Fig. 1.2). Downward flashes exhibit downward branching, while upward flashes are branched upward. Upward lightning discharges (types (b) and (d) in Fig. 1.2) are thought to occur only from tall objects (higher than 100 m or so) or from

Transpose

Transpose

Table 2.2 Number, N = 200 p(n), of houses out of a total of 200 (percentage if divided by 2) expected to be struck by lightning n times over T years ($N_g = 4\ km^{-2}\ yr^{-1}$; $A = 1200\ m^2$)

Number of years of observation, T	Number of times struck by lightning, n				
	0	1	2	3	>3
10	191	9	0	0	0
20	182	17	1	0	0
30	173	25	2	0	0
40	165	32	3	0	0
50	157	38	5	0	0
60	150	43	6	1	0
70	143	48	8	1	0
80	136	53	10	1	0
90	130	56	12	2	0
100	124	60	14	2	0

a region characterized by a moderate ground flash density of $4\ km^{-2}\ yr^{-1}$ and having an area of $10 \times 20\ m^2$ and a height of 5 m so that the equivalent attractive distance is about 10 m (extrapolating Eq. 2.6 with $\alpha = 2$ and $\beta = 1$ to a structure height of 5 m), the approximate equivalent attractive area is $30 \times 40 = 1200\ m^2$. Such a house is expected to be struck by lightning $(1200\ m^2)\ (10^{-6}\ km^2\ m^{-2})\ (4\ km^{-2}\ yr^{-1}) = 4.8 \times 10^{-3}$ times a year, or about once every 200 years on average. Another way to think of this lightning incidence is that, in this region, one of every 200 houses will be struck each year, on average.

The probability of a structure, represented by its equivalent attractive area A, to be struck exactly 0, 1, 2, 3, … n times in T years can be estimated using the Poisson probability distribution,

$$p(n) = (Z^n/n!)\exp(-Z) \qquad (2.8)$$

Delete slash here.

where $Z = AN_gT = N_d T$, the average number of strikes expected over T years, provided that N_g remains constant. Continuing the previous example, Table 2.2 gives the number of houses, out of a total of 200, expected to be struck by lightning n times over T years, as predicted by Eq. 2.8. Each number is found as the product of the total number of houses, 200, and p(n) from Eq. 2.8 with subsequent rounding off to the nearest integer. In two cases (n = 1; T = 80 yr and T = 100 yr) the rounded-off number was increased by 1 in order to assure that the sum of numbers in each row is 200, the total number of houses considered. It follows from Table 2.2 that, for example, over a 60-year period 150 houses will not be struck at all, 50 (43 + 6 + 1) will receive at least one strike, six houses will be struck twice, and one house will be struck three times. If $N_g = 12\ km^{-2}\ yr^{-1}$, characteristic of some areas in Florida, then over a period of 60 years (perhaps the lifetime of a house) only 84 houses out of the 200 will receive no lightning strikes, and 11 houses will be struck three times or more.

dominant, and the total electric field (the sum of the contributions from the two charges) changes its polarity. The distance at which the two contributions are equal to each other (add to zero) is called the "reversal distance." For the case of two vertically-stacked charges of equal magnitude but opposite polarity, the reversal distance, D_0, is given by

$$D_0 = [(H_P H_N)^{2/3}(H_P{}^{2/3} + H_N{}^{2/3})]^{1/2} \quad (3.4)$$

where H_P and H_N are the heights of the positive and negative charges, respectively. Thus, for a positive dipole, one might expect that at close ranges the total electric field is negative (the closer negative charge is more "visible"), while at far ranges it is positive (the larger-elevation-angle positive charge is more "visible").

The electric field at ground level due to the system of three charges (a vertical tripole) shown in Fig. 3.2a, computed assuming that the middle negative and top positive charges are 7 and 12 km above ground, respectively, each having a magnitude of 40 C, and that the bottom positive charge is at 2 km and has a magnitude of 3 C, is shown in Fig. 3.2c. An upward-directed electric field in this chapter is defined as positive (the so-called physics sign convention, which corresponds to a coordinate system with the vertical axis directed

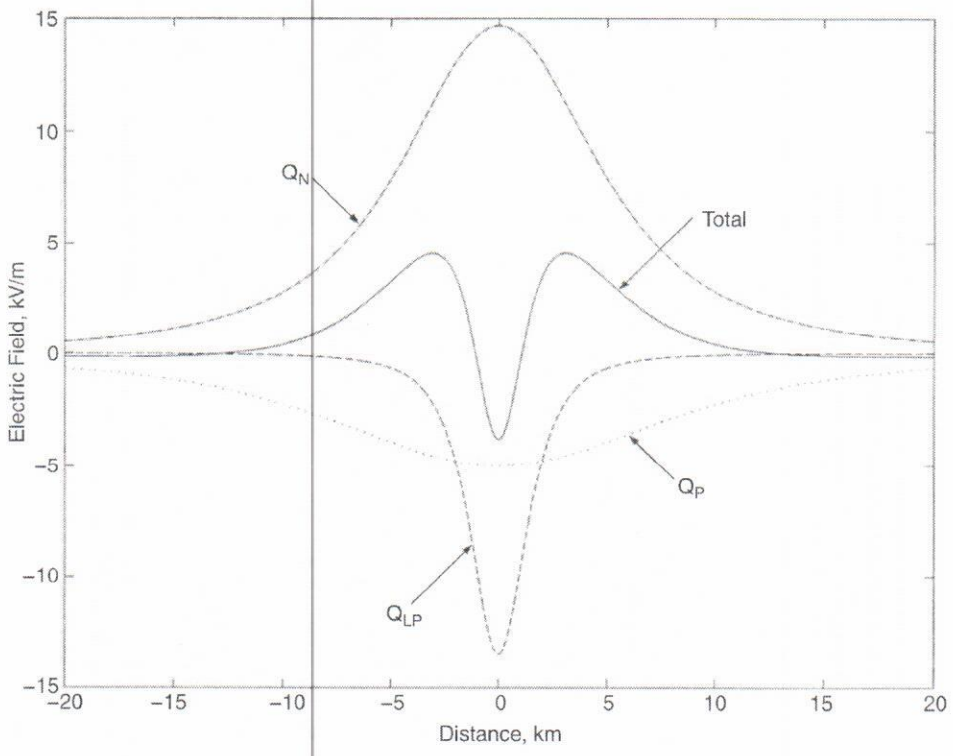

Fig. 3.2c Electric field at ground due to the vertical tripole shown in Fig. 3.2a, labeled Total, as a function of distance r from the axis (at r = 0) of the tripole. Also shown are the contributions to the total electric field from the three individual charges of the tripole. An upward directed electric field is defined as positive (physics sign convention). © Vladimir A. Rakov and Martin A. Uman 2003, published by Cambridge University Press, reprinted with permission.

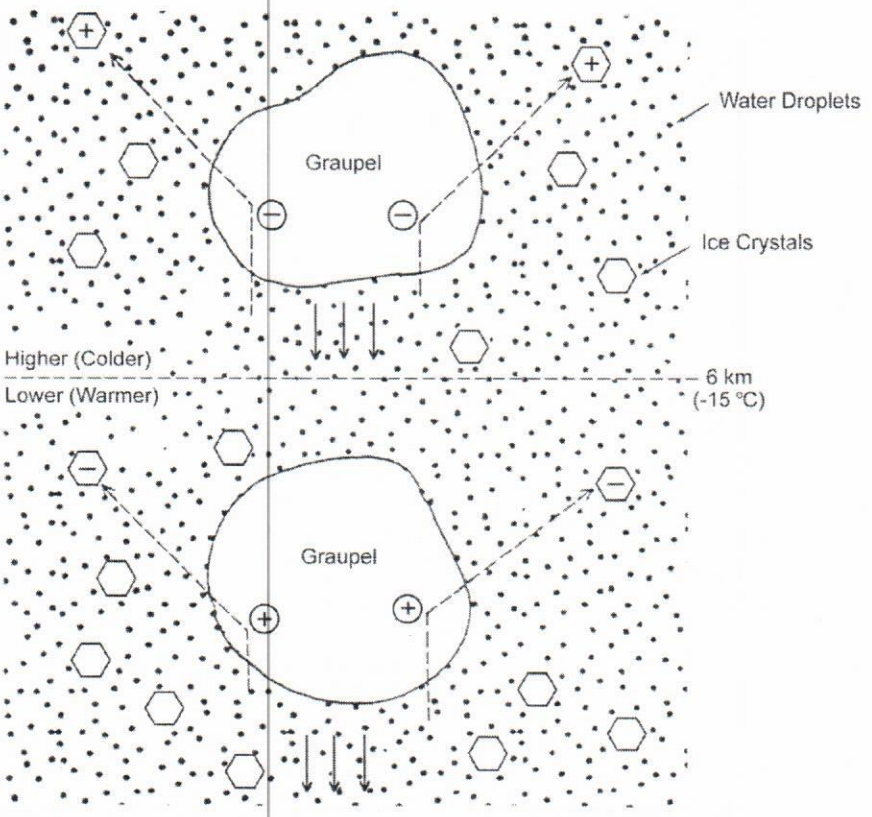

Fig. 3.9 Schematic representation of the graupel-ice mechanism of cloud electrification, in which the charge transfer occurs via collision of graupel with small ice crystals in the presence of supercooled water droplets. It is assumed that the reversal temperature T_R is −15°C, and that it occurs at a height of 6 km. © Vladimir A. Rakov and Martin A. Uman 2003, published by Cambridge University Press, reprinted with permission.

lower positive charge region in the cloud, discussed in Section 3.5. Figure 3.10 shows the charge acquired by a simulated riming hail particle during collisions with ice crystals as a function of temperature, from the laboratory experiments of Jayaratne et al. (1983). In general, the sign and magnitude of the electric charge separated during collisions between vapor-grown ice crystals and graupel depends on, besides the temperature, a number of other factors including cloud water content, ice crystal size, relative velocity of the collisions, chemical contaminants in the water, and supercooled droplet size spectrum.

It is believed that the polarity of the charge that is separated in ice-graupel collisions is determined by the rates at which the ice and graupel surfaces are growing. The surface that is growing faster acquires a positive charge. There is no consensus on the detailed physics involved. One reasonable model has been proposed by Baker and Dash (1994). They have suggested that there might be a liquid-like layer (LLL) on ice surfaces and, if so, there

Rakov et al. (1992) proposed the following empirical formula (linear regression equation) to estimate the negative return-stroke peak current, I, from the initial electric field peak, E, and distance, r, to the lightning channel:

$$I = 1.5 - 0.037Er \tag{4.11}$$

where I is in kA and taken as negative, E is positive and in V/m, and r is in km. Equation 4.11 was derived using data for 28 triggered-lightning strokes acquired by Willett et al. (1989) at the Kennedy Space Center (KSC), Florida. The fields were measured at about 5 km and their initial peaks were assumed to be pure radiation. The currents were directly measured at the lightning channel base.

Lightning peak currents can also be estimated using the radiation-field-to-current conversion equation based on the transmission line (TL) model (Uman and McLain, 1969), which for the electric field is given by

$$I = \frac{2\pi\varepsilon_0 c^2 r}{v} E \tag{4.12}$$

where ε_0 is the permittivity of free space, c is the speed of light, and v is the return-stroke speed (assumed to be constant). The return-stroke speed is generally unknown and its range of variation is from one-third to two-thirds of the speed of light. Both I and E in Equation 4.12 are absolute values. The equation is thought to be valid for instantaneous values of E and I at early times (for the initial rising portion of the waveforms, including the peak).

The US National Lightning Detection Network (NLDN) uses an empirical formula, based on triggered-lightning data, to estimate the return-stroke peak current from the measured magnetic field peak and distance to the strike point determined using data from multiple sensors. The conversion procedure includes compensation for the field attenuation due to its propagation over lossy ground (Cummins and Murphy, 2009). The procedure has been validated using rocket-triggered lightning data and tower-initiated lightning data. Since strokes in triggered and tower-initiated lightning are similar to subsequent strokes in natural lightning, the results are applicable only to subsequent strokes. Peak-current estimation errors for negative first strokes and for positive lightning are presently unknown.

Mallick et al. (2013) compared peak currents obtained using the three methods outlined above with directly measured peak currents for 93 negative strokes in 24 lightning flashes triggered using the rocket-and-wire technique at Camp Blanding, Florida, in 2008–2010. The empirical formula (Eq. 4.11), based on data from the KSC, tended to overestimate peak currents, whereas the NLDN-reported peak currents were on average underestimates. The field-to-current conversion equation based on the transmission line model gave the best match with directly measured peak currents for return-stroke speeds between $c/2$ and $2c/3$ (1.5 and 2×10^8 m/s, respectively).

NLDN-reported peak currents vs. directly measured currents for negative strokes in rocket-triggered lightning are shown in Fig. 4.34. Median absolute current estimation error is 14 percent. Similar scatter plots were reported for peak currents estimated by the NLDN-type European Cooperation for Lightning Detection (EUCLID) network vs. those directly measured at the Gaisberg Tower in Austria.

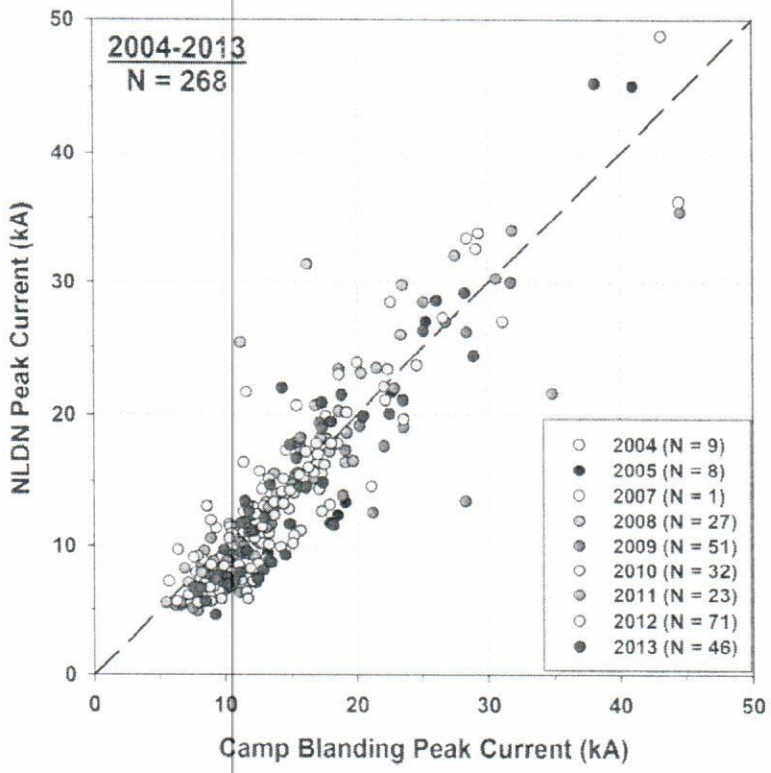

NLDN-reported peak current versus peak current directly measured for 268 return strokes in lightning flashes triggered at Camp Blanding, Florida, in 2004–13. The slanted broken line (slope = 1) is the locus of the points for which the NLDN-reported peak currents and the directly measured peak currents are equal. The NLDN tends to underestimate the peak current (by about 10 percent, on average). Adapted from Mallick et al. (2014).

4.6 Subsequent leader

Return strokes subsequent to the first are usually initiated by dart leaders. An example of a dart leader/return stroke sequence imaged by a streak camera is found in Fig. 4.28a. The negatively sloped image on the left is due to the dart leader, and the brighter image on the right is due to the return stroke. As seen in Fig. 4.28a, the dart leader appears, unlike the stepped leader (see Fig. 4.9), to move continuously, that is, the lowest portion of the leader channel, called the dart, remains luminous during the channel extension from the cloud to ground. Luminosity versus time at different heights above ground corresponding to the streak photograph in Fig. 4.28a is shown for the entire visible channel and for the bottom 480 m in Figs. 4.28b and c, respectively. Many subsequent return strokes (more than one-third of second strokes in channels that are not too old) are initiated by leaders that exhibit pronounced stepping in the bottom portion of the channel. Such leaders produce regular pulse sequences that are observed just prior to the return-stroke pulse in distant electric or

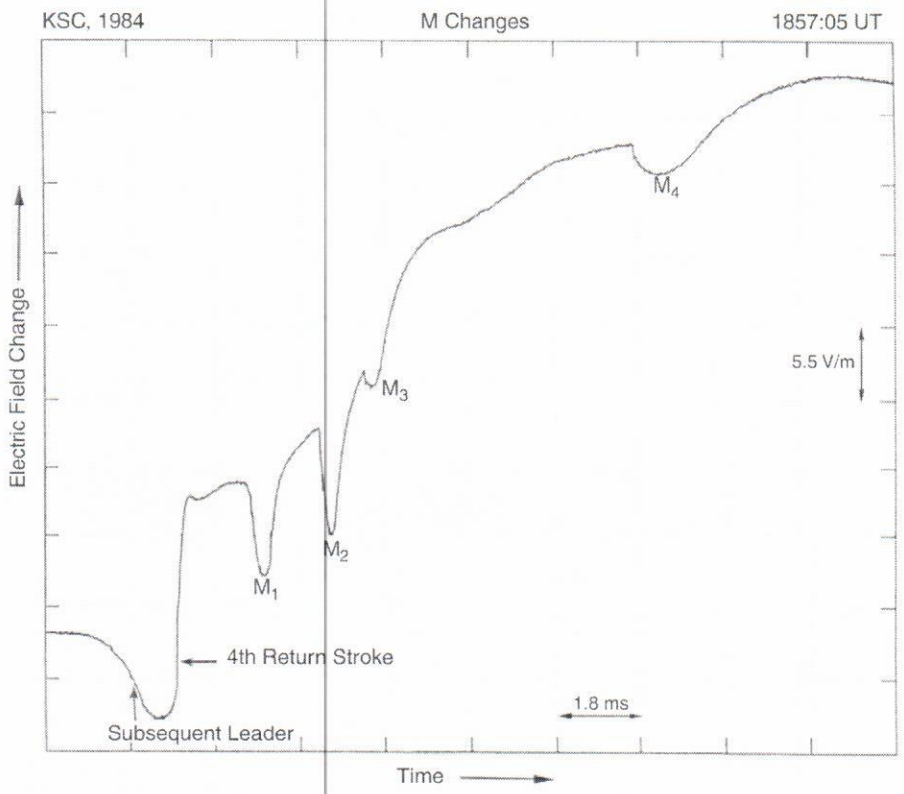

Fig. 4.41 Hook-shaped electric field changes due to M components (labeled M_1 through M_4) during the continuing current initiated by the fourth return stroke in a flash that occurred in Florida at a range of probably 5 km. A positive field change (atmospheric electricity sign convention, according to which a downward-directed electric field or field change is defined as positive) deflects upward. Adapted from Rakov et al. (1992a).

Fig. 4.40a), comparable to current peaks of smaller return strokes. An electric field record showing signatures of M-components is presented in Fig. 4.41 (see also electric field signatures labeled "M-change" and corresponding optical images in Fig. 4.4, the upper set of records).

Rakov et al. (1995) have proposed a mechanism for the "classical" M-component. According to this mechanism, an M component is essentially a guided-wave process that involves a downward progressing incident wave (the analog of a leader) and an upward progressing wave that is a reflection of the incident wave from the ground (the analog of a return stroke). Ground is sensed by the incident M-wave as essentially a short circuit, so the reflection coefficient for current at ground is close to +1, and the reflection coefficient for the associated charge density is close to −1. Because the reflection coefficients for the traveling waves of current and charge density are positive and negative, respectively, the incident and reflected waves of current (which determine the close magnetic fields) add at each channel section, while the incident and reflected waves of charge density (which

5 Calculation of lightning electromagnetic fields

5.1 General approach

The electric field intensity, $\overline{E}$, and magnetic flux density, $\overline{B}$, are usually found using the scalar, ϕ, and vector, $\overline{A}$, potentials as follows:

$$\overline{E} = -\nabla\phi - \partial\overline{A}/\partial t \tag{5.1}$$

$$\overline{B} = \nabla \times \overline{A} \tag{5.2}$$

The potentials, ϕ and $\overline{A}$, are related to the volume charge density, ρ, and current density, $\overline{J}$, respectively, by

$$\phi = \frac{1}{4\pi\varepsilon_0}\int_{V'}\frac{\rho(\overline{r}',\ t - R/c)}{R}\,dV' \tag{5.3}$$

$$\overline{A} = \frac{\mu_0}{4\pi}\int_{V'}\frac{\overline{J}(\overline{r}',\ t - R/c)}{R}\,dV' \tag{5.4}$$

where ε_0 and μ_0 are the electric permittivity and magnetic permeability of free space (also applicable to air), respectively, V' is the source volume, dV' is the differential source volume, $\overline{r}'$ and $\overline{r}$ are the radius (position) vectors of the differential source volume and observation (field) point, respectively, t is the time, c is the speed of light, and R is the inclined distance between the differential source volume and the observation point. The ratio R/c is the time required for electromagnetic signals to propagate from the source to the field point, and t – R/c is referred to as the retarded time. Note that $\overline{E}$, $\overline{B}$, $\overline{A}$, and $\overline{J}$ are vectors and ϕ and ρ are scalars.

The scalar and vector potentials are related by the Lorentz condition:

$$\nabla \cdot \overline{A} + c^{-2}\partial\phi/\partial t = 0 \tag{5.5}$$

which is equivalent to the continuity equation relating ρ and $\overline{J}$:

$$\nabla \cdot \overline{J} + \partial\rho/\partial t = 0 \tag{5.6}$$

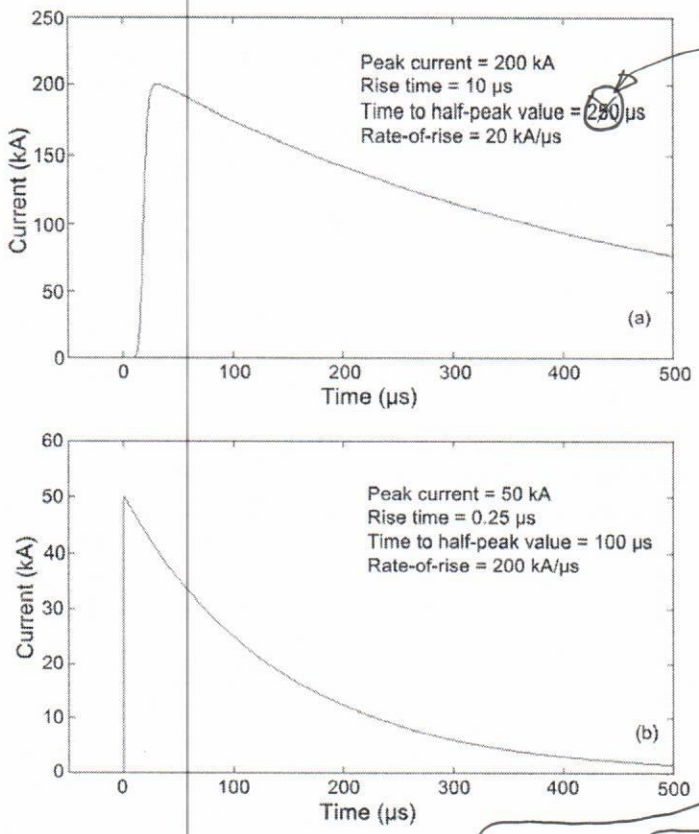

Fig. 5.3 Current waveforms recommended by the IEC 62305–1 (2010) for (a) first and (b) subsequent return strokes. The rise-time was measured between the 10% and 90% of peak value levels on the front part of the waveform. The rate-of-rise is the ratio of 0.8 of the peak value and 10–90% rise-time. The time to half-peak value was measured between the peak and half-peak value on the tail part of the waveform. Drawing by Vijaya B. Somu and Potao Sun.

electric field at and below the ground surface is associated with a radial current flow and resultant ohmic losses in the earth. A nonzero horizontal electric field on the ground surface makes the total electric field vector tilted relative to the vertical. The tilt is in the direction of propagation if the vertical electric field component is directed upward and in the direction opposite to the propagation direction if the vertical electric field component is directed downward, with the vertical component of the Poynting vector (power flow per unit area) being directed into the ground in both cases. Propagation effects include the preferential attenuation of the higher-frequency components in the vertical electric field and the azimuthal magnetic field waveforms.

Aoki et al. (2015) studied in detail the effects of finite ground conductivity on lightning electric and magnetic fields, using the 2D finite-difference time-domain method. Their distance range was from 5 to 200 km and the ground conductivity range from 0.1 mS/m (10^{-4} S/m) to infinity. They used the MTLL return-stroke model (Chapter 6) and considered

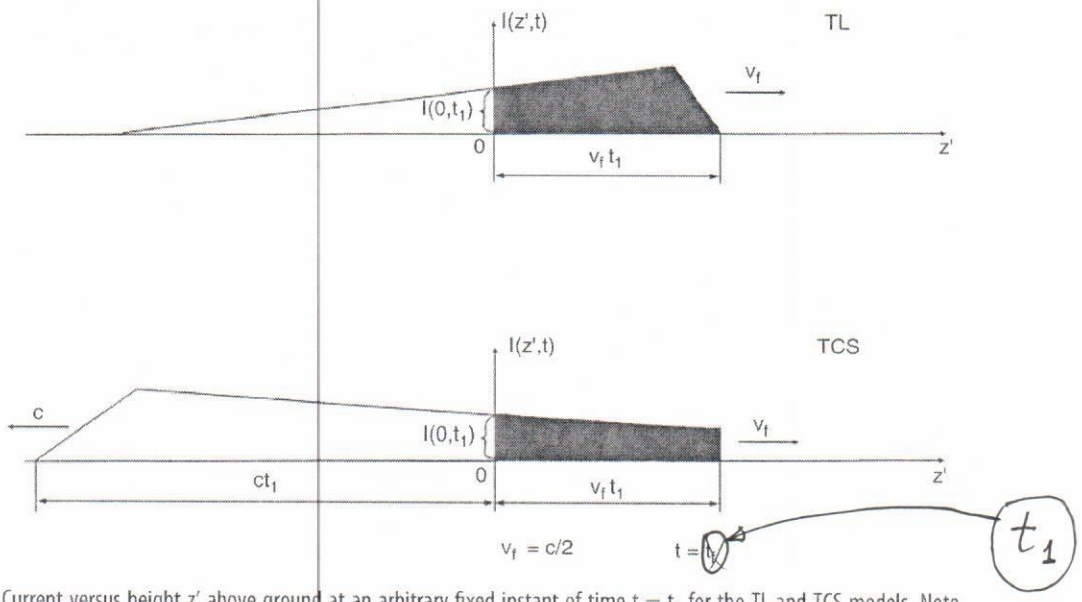

Fig. 6.2 Current versus height z′ above ground at an arbitrary fixed instant of time $t = t_1$ for the TL and TCS models. Note that the current at $z' = 0$ and v_f are the same for both models. Adapted from Rakov (1997).

line labeled v_f. The current-wave speed is represented by the line labeled v which coincides with the vertical axis for the BG model and with the v_f line for the TL model. Shown for each model are current versus time waveforms at the channel base ($z' = 0$) and at heights z'_1 and z'_2. Because of the finite front propagation speed v_f, current at a height, say, z'_2 begins with a delay z'_2/v_f with respect to the current at the channel base. The dark portion of the waveform indicates the current that actually flows through a given channel section, the blank portion being shown for illustrative purpose only. As seen in Fig. 6.1, the TCS, BG, and TL models are characterized by different current profiles along the channel, the difference being, from a mathematical point of view, due to the use of different values of v (listed in Table 6.1) in the generalized Eq. 6.1 with $P(z') = 1$. It also follows from Fig. 6.1 that if the channel-base current were a step function, the TCS, BG, and TL models would be characterized by the same current profile along the channel, although established in an apparently different way in each of the three models. The relation between the TL and TCS models is further illustrated in Fig. 6.2 which shows that the spatial current wave moves in the positive z′ direction for the TL model and in the negative z′ direction for the TCS model. Note that in Fig. 6.2 the current at ground level ($z' = 0$) and the upward moving front speed v_f are the same for both the TL and the TCS models. As in Fig. 6.1, the dark portion of the waveform indicates the current that actually flows in the channel, the blank portion being shown for illustrative purpose only.

The most used engineering models can be grouped in two categories: the transmission-line-type models and the traveling-current-source-type models, summarized in Tables 6.2 and 6.3, respectively. Each model in Tables 6.2 and 6.3 is represented by both current and

without attenuation or distortion. Such an extension results in a second current wavefront which propagates from the top of the object toward ground at the speed of light, produces reflection on its arrival there, and is allowed to bounce between the top and bottom ends of the object and, in general, produce transmitted waves at either end. The transient behavior of tall objects under direct lightning strike conditions can be illustrated as follows. For the simple example of a non-ideal current source (ideal current source in parallel with source impedance) attached to the top of the object (see Fig. 4.30b) generating a step-function current wave, the magnitude of the wave injected into the object depends on the characteristic impedance of the object. Specifically, the ideal source current initially divides between the source impedance and the characteristic impedance of the object. However, after a sufficiently long period of time, the current magnitude at any point on the object will be equal to the magnitude of current that would be injected directly into the grounding impedance of the object from the same current source in the absence of the object. In other words, at late times, the ideal source current will in effect divide between the source impedance and the grounding impedance, as if the strike object were not there. Note that the above example applies only to a step-function current wave, the current distribution along the object being more complex for the case of an impulsive current waveform characteristic of the lightning return stroke. If the lightning current wave round-trip time on the strike object is appreciably longer than the rise time of current measured at the top of the object, the current peak reflected from the ground is separated from the incident-current peak in the overall current waveform, at least in the upper part of the object.

Model-predicted lightning electromagnetic environment in the presence of tall (electrically long) strike object was studied by many researchers. According to Baba and Rakov (2007b), for a typical subsequent stroke, the vertical electric field due to a lightning strike to a 100 m-high object is expected to be reduced relative to that due to the same strike to flat ground at distances ranging from 30 m to 200 m from the object and enhanced at distances greater than 200 m. The azimuthal magnetic field for the tall object case is larger than that for the flat ground case at any distance. Beyond about 3 km the field peak is essentially determined by its radiation component and the so-called far-field enhancement factor becomes insensitive to distance change and expected to be equal to about 2.3.

Note that when the shortest significant wavelength in the lightning current is much longer than the height of the strike object, there is no need to consider the distributed-circuit behavior of such an object. For example, if the minimum significant wavelength is 300 m (corresponding to a frequency of 1 MHz), objects whose heights are about 30 m or less may be considered as lumped, in most cases as a short circuit between the lightning channel base and grounding impedance of the object (see Fig. 4.30a).

6.5 Testing model validity

The overall strategy in testing the validity of engineering models is illustrated in Fig. 6.4. For a given set of input parameters, including $I(0,t)$ and v_f, the model is used to find the distribution of current $I(z',t)$ along the channel, which is then used for computing electric and magnetic fields (using equations found in Chapter 5) at different distances from the

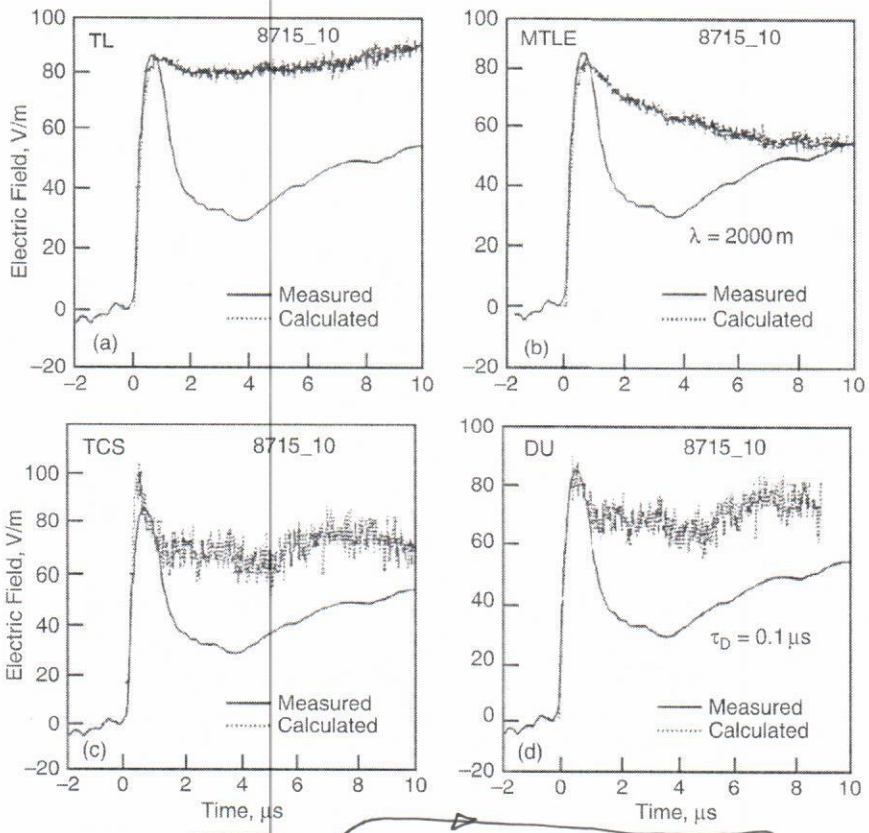

Fig. 6.10 The vertical electric fields ("noisy" dotted lines) calculated using the TL, MTLE, TCS, and DU models, shown together with the measured field (solid lines) at about 5 km for the return stroke whose measured current at the channel base and the measured return-stroke speed are given in Fig. 6.9. Adapted from Thottappillil and Uman (1993).

each predicted the measured initial electric field peaks with an error whose mean absolute value was about 20 percent, while the TCS model had a mean absolute error of about 40 percent. From the standpoint of the overall field waveforms at 5 km, all the tested models should be considered less than adequate.

Schoene et al. (2003b) tested the TL and TCS models by comparing the first microsecond of model-predicted electric and magnetic field waveforms and field derivative waveforms at 15 m and 30 m with the corresponding measured waveforms from triggered-lightning return strokes. The electric and magnetic fields were calculated from Eqs. 5.7 and 5.8 given the measured current or current derivative at the channel base, an assumed return stroke front speed (three values, $v = 1 \times 10^8$ m/s, $v = 2 \times 10^8$ m/s, and $v = 2.99 \times 10^8$ m/s, were considered), and the temporal and spatial distribution of the channel current specified by the return-stroke model. This was a somewhat lesser testing method than the "individual approach" discussed above, since the speeds were not measured and had to be assumed. The TL model was found to work reasonably well in predicting the measured electric and magnetic fields (and field derivatives) at 15 m and 30 m if return stroke speeds during the

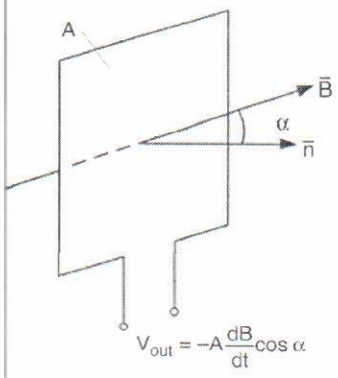

Fig. 7.8 Illustration of the principle of operation of the loop antenna. Drawing by Potao Sun.

between the magnetic flux density vector and the normal to the plane of the loop, to be constant over that area, we can express the magnitude of induced voltage as follows:

$$V = A\frac{dB_n}{dt} \tag{7.3}$$

When $\cos\alpha = 1$ ($\alpha = 0$), the induced voltage is maximum, and when $\cos\alpha = 0$ ($\alpha = 90°$), the induced voltage is zero. It follows that a vertical loop antenna in a fixed position is directional in that the magnitude of voltage induced across its terminals is a function of the direction to the source, and two such antennas with orthogonal planes can be used for magnetic direction finding (see Chapter 8). In order to obtain the horizontal (azimuthal) component of magnetic field, which is the dominant component for essentially vertical lightning channels, two vertical loop antennas are required, unless the direction to the lightning channel is known (for example, in the case of rocket-triggered lightning). Since the signal at the output of a loop antenna is proportional to the magnetic field derivative, the signal must be integrated to obtain the field. This can be accomplished using either an RC or RL circuit, or the measured field derivative signal can be integrated numerically. We will consider below the case of RC integrator.

In the following, we will assume that B is normal to the plane of the loop antenna ($\alpha = 0$), so that $B = B_n$. The voltage induced at the terminals of a loop antenna is the open-circuit voltage, $Aj\omega B$, and hence it can be used for building the Thevenin equivalent circuit of the antenna. The source impedance is predominantly inductive, $j\omega L$. The overall equivalent circuit including, besides the antenna, the RC integrator and input impedance (input resistance in parallel with input capacitance) of the recorder is shown in Fig. 7.9.

In contrast with the electric field antenna (see Fig. 7.2), the integrating capacitor in Fig. 7.9 has two discharge paths, one through the input resistance of the recorder (similar to Fig. 7.2) and the other through resistor R of the integrating circuit and the source (the ideal voltage source has zero impedance). As a result, there are three conditions for undistorted recording of magnetic field with the measuring system shown in Fig. 7.9. The first one, $R >> 1/\omega C$ ($\omega >> 1/(RC)$; C_{in} is neglected), determines the lower frequency limit and is equivalent to the $\Delta t << \tau$ ($\tau = RC$) condition. The second one, $R >> \omega L$ ($\omega << R/L$),

2010). Maximizing the detection efficiency for cloud flashes appears to be the primary focus of this system. Peak currents for processes in cloud flashes, in-cloud processes (e.g. preliminary breakdown) in CG flashes, and CG strokes are estimated assuming direct proportionality between the peak current and peak electric field and inverse distance dependence of field peak.

Mallick et al. (2015) have evaluated the performance characteristics of the ENTLN using, as ground truth, data for 245 negative return strokes in 57 flashes triggered from June 2009 to August 2012 at Camp Blanding, Florida. The performance characteristics were determined both for the ENTLN processor that had been in service at the time of acquiring triggered-lightning data (June 2009 to August 2012) and for the new ENTLN processor, introduced in November 2012. So, evaluation for the new processor simulates ENTLN output as if the new processor were in service from June 2009 to August 2012. For the same ground-truth dataset and the same evaluation methodology, different performance characteristics for those two processors were obtained. For the old processor, flash detection efficiency was 77 percent, stroke detection efficiency was 49 percent, fraction of misclassified events was 61 percent, median location error was 631 m, and median absolute current estimation error was 51 percent. For the new processor, flash detection efficiency was 89 percent, stroke detection efficiency was 67 percent, fraction of misclassified events was 54 percent, median location error was 760 m, and median absolute current estimation error was 19 percent.

8.4.6 World Wide Lightning Location Network (WWLLN), 6–18 kHz

The WWLLN utilizes the time-of-group-arrival (TOGA) method (see Section 8.2.5) to locate lightning events. As of March 2012, WWLLN employed 57 sensors located on all continents, although, according to Dowden et al. (2002), global coverage could be in principle provided by as few as 10 sensors. Distances between the sensors are up to thousands of kilometers. Presently, only those lightning events that triggered at least five sensors and that had residuals (uncertainties in the stroke timing) less than or equal to 30 μs are regarded as located with acceptable accuracy.

In their study of WWLLN performance characteristics, Abarca et al. (2010) used NLDN data as the ground truth and found that the CG flash detection efficiency increased from about 3.88 percent in 2006–7 to 10.3 percent in 2008–9, as the number of sensors increased from 28 in 2006 to 38 in 2009. For events with NLDN-reported peak currents of 130 kA or higher, the detection efficiency was reported to be 35 percent. The average location error was estimated to be 4–5 km. Hutchins et al. (2012a) developed a model to compensate for the uneven global coverage of the WWLLN. It is known that field peaks at distances >700 km or so are due to ionospheric reflections rather than the ground wave. Interaction of lightning signals with the ionosphere spectrally distorts the field waveform so that it is not straightforward to infer the peak current and even polarity of lightning. Nevertheless, Hutchins et al. (2012b) developed a method to convert the stroke-radiated power in the 6–18 kHz band to peak current.

Mallick et al. (2014) evaluated the performance characteristics of the WWLLN using rocket-triggered lightning data acquired at Camp Blanding, Florida, in 2008–13. The flash

and stroke detection efficiencies were 8.8 percent and 2.5 percent, respectively. The stroke detection efficiency for strokes with peak current ≥25 kA was 29 percent. The median location error was 2.1 km. The median absolute error in WWLLN peak currents estimated from the empirical formula of Hutchins et al. (2012b) was 30 percent.

8.4.7 Global Lightning Dataset (GLD360), 300 Hz–48 kHz

The Global Lightning Dataset (GLD360), also referred to as the Global Lightning Detection Network (GLDN), employs an unspecified number of VLF sensors strategically placed around the world. As stated in Section 8.2.5, locations are obtained using both TOA and MDF methods in conjunction with a lightning waveform recognition algorithm. A lightning event must be detected by at least three sensors to be located. The system does not distinguish between ground and cloud lightning events.

Demetriades et al. (2010) evaluated the GLD360 performance characteristics using NLDN data as the ground truth and found that the CG flash detection efficiency was 86–92 percent, and the median location error was 10.8 km. From a similar study, but using the Brazilian lightning detection network, Naccarato et al. (2010) reported the CG flash detection efficiency of 16 percent and the mean location error of 12.5 km. GLD360 performance in Europe in May–September 2011 was compared with that of the networks participating in the European Cooperation for Lightning Detection (EUCLID) by Ponjola and Makela (2013). Poelman et al. (2013), using electric field measurements in conjunction with high-speed video recordings for 210 strokes in 57 negative CG flashes in Belgium, estimated the flash and stroke detection efficiencies to be 96 and 70 percent, respectively. They also estimated the median location error of 1.3 km (N = 134) relative to EUCLID locations. Said et al. (2013), using NLDN data as the ground truth, estimated the ground flash detection efficiency of 57 percent and median location error of 2.5 km.

The GLD360 also reports the peak current (inferred from the measured magnetic field peak) and polarity. The latter is determined via the cross-correlation with the bank of "canonical" waveforms. Said et al. (2013) estimated the mean and geometric mean errors in peak current estimates relative to NLDN-reported peak currents to be 21 and 6 percent, respectively. They also found that for 96 percent of matched events, GLD360 reported the same polarity as the NLDN.

Mallick et al. (2014b) used rocket-triggered lightning data acquired in 2011–13 at Camp Blanding, Florida, to evaluate the GLD360 performance characteristics. The flash and stroke detection efficiencies were 67 and 37 percent, respectively. Out of 75 detected strokes, one (1.3 percent) was reported with incorrect polarity. The median location error was 2.0 km, and the median absolute current estimation error was 27 percent.

8.5 Summary

There exists a variety of lightning locating techniques that are based on the detection of lightning radio-frequency electromagnetic signals, with accurate locating being possible

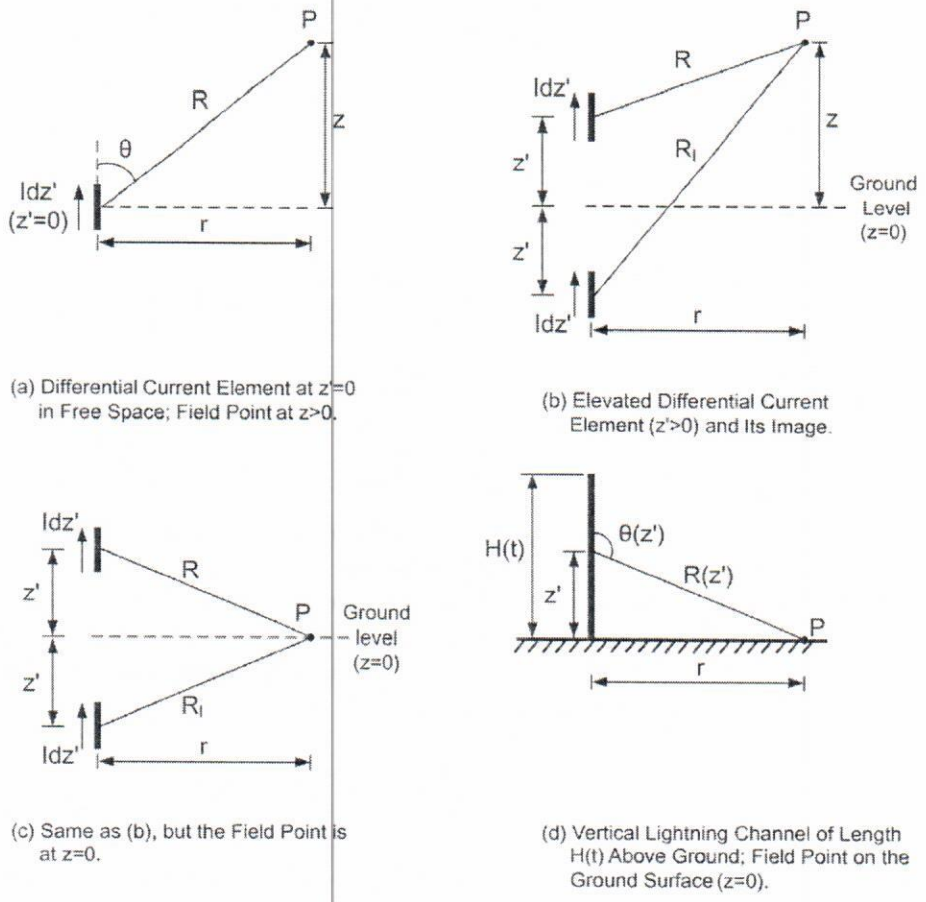

Fig. A3.1 Four configurations used in deriving exact lightning electric and magnetic field equations. Drawing by Potao Sun.

$$d\overline{B} = \nabla \times \overline{A} = -\frac{\partial A_z}{\partial r}\overline{a}_\phi = -\frac{\mu dz'}{4\pi}\frac{\partial}{\partial r}\left[\frac{I(t - R/c)}{R}\right]\overline{a}_\phi \qquad (A3.2)$$

Since $R = (r^2+z^2)^{1/2}$, we use the product rule to take the derivative with respect to r. Then, noting that the derivative of 1/R with respect to r is $-r/R^3$, we get

$$d\overline{B} = -\frac{\mu dz'}{4\pi}\left[\frac{1}{R}\frac{\partial I(t - R/c)}{\partial r} + I(t - R/c)\left(-\frac{r}{R^3}\right)\right]\overline{a}_\phi \qquad (A3.3)$$

The spatial derivative $\partial I/\partial r$ can be converted to the time derivative $\partial I/\partial t$ by comparing the following two equations, in which the chain rule was used to take the partial derivatives with respect to r and t and I′ stands for the derivative of I with respect to (t – R/c):

$$\frac{\partial I(t - R/c)}{\partial r} = \frac{\partial I(t - R/c)}{\partial (t - R/c)} \cdot \frac{\partial (t - R/c)}{\partial r} = -\frac{r}{cR} I'(t - R/c)$$

Assemble the results:

$$\begin{aligned}
\bar{a}_r \frac{\partial}{\partial r}(\nabla \cdot \bar{A}) &= \frac{\mu_0 dz'}{4\pi}\left\{\frac{1}{R}\left[\frac{zr}{cR^3}\frac{\partial I(t-R/c)}{\partial t}+\frac{zr}{c^2R^2}\frac{\partial^2 I(t-R/c)}{\partial t^2}\right]\right.\\
&\quad +\left(-\frac{r}{R^3}\right)\left[-\frac{z}{cR}\frac{\partial I(t-R/c)}{\partial t}\right]+\left(-\frac{z}{R^3}\right)\left[-\frac{r}{cR}\frac{\partial I(t-R/c)}{\partial t}\right]\\
&\quad \left.+\frac{3zr}{R^5}I(t-R/c)\right\}\bar{a}_r\\
&= \frac{\mu_0 dz'}{4\pi}\left[\frac{3rz}{R^5}I(t-R/c)+\frac{3rz}{cR^4}\frac{\partial I(t-R/c)}{\partial t}+\frac{rz}{c^2R^3}\frac{\partial^2 I(t-R/c)}{\partial t^2}\right]\bar{a}_r
\end{aligned}$$

$$\begin{aligned}
\bar{a}_z \frac{\partial}{\partial z}(\nabla \cdot \bar{A}) &= \frac{\mu_0 dz'}{4\pi}\left\{\frac{1}{R}\left[\left(-\frac{1}{cR}+\frac{z^2}{cR^3}\right)\frac{\partial I(t-R/c)}{\partial t}+\frac{z^2}{c^2R^2}\frac{\partial^2 I(t-R/c)}{\partial t^2}\right]\right.\\
&\quad -\frac{z}{R^3}\left[-\frac{z}{cR}\frac{\partial I(t-R/c)}{\partial t}\right]-\frac{1}{R^3}I(t-R/c)+\frac{3z^2}{R^5}I(t-R/c)\\
&\quad \left.-\frac{z}{R^3}\left[-\frac{z}{cR}\frac{\partial I(t-R/c)}{\partial t}\right]\right\}\bar{a}_z\\
&= \frac{\mu_0 dz'}{4\pi}\left[\left(\frac{3z^2}{R^5}-\frac{1}{R^3}\right)I(t-R/c)+\left(\frac{3z^2}{cR^4}-\frac{1}{cR^2}\right)\frac{\partial I(t-R/c)}{\partial t}\right.\\
&\quad \left.+\frac{z^2}{c^2R^3}\frac{\partial^2 I(t-R/c)}{\partial t^2}\right]\bar{a}_z
\end{aligned}$$

Make this bracket large.

Thus, the r- and z-components of $\nabla\phi$ become:

r-component

$$\begin{aligned}
\nabla\phi_r &= -c^2\int_{-\infty}^{t}\bar{a}_r\frac{\partial}{\partial r}(\nabla\cdot\bar{A})d\tau = -\frac{dz'}{4\pi\varepsilon_0}\left[\frac{3rz}{R^5}\int_0^t I(\tau-R/c)d\tau\right.\\
&\quad \left.+\frac{3rz}{cR^4}I(t-R/c)+\frac{rz}{c^2R^3}\frac{\partial I(t-R/c)}{\partial t}\right]\bar{a}_r
\end{aligned}$$

z-component

$$\begin{aligned}
\nabla\phi_z &= -c^2\int_{-\infty}^{t}\bar{a}_z\frac{\partial}{\partial z}(\nabla\cdot\bar{A})d\tau = -\frac{dz'}{4\pi\varepsilon_0}\left[\left(\frac{3z^2}{R^5}-\frac{1}{R^3}\right)\int_0^t I(\tau-R/c)d\tau\right.\\
&\quad \left.+\left(\frac{3z^2}{cR^4}-\frac{1}{cR^2}\right)I(t-R/c)+\frac{z^2}{c^2R^3}\frac{\partial I(t-R/c)}{\partial t}\right]\bar{a}_z
\end{aligned}$$

Make these brackets larger.

where the lower integration limit is changed from $-\infty$ to zero and c^2 is replaced with $(\mu_0\varepsilon_0)^{-1}$.

Finally, the time derivative of $\bar{A}$ is

$$\frac{\partial \bar{A}}{\partial t} = \frac{\partial}{\partial t}\left[\frac{\mu_0 dz' I(t - R/c)}{4\pi R}\bar{a}_z\right] = \frac{dz'}{4\pi\varepsilon_0}\left(\frac{1}{c^2 R}\frac{\partial I(t - R/c)}{\partial t}\right)\bar{a}_z \qquad \text{z-component}$$

where μ_0 is replaced with $(\varepsilon_0 c^2)^{-1}$.

The electric field intensity expression has three terms and is given by

$$d\bar{E} = -\nabla\phi_r - \nabla\phi_z - \partial\bar{A}/\partial t \qquad \text{(A3.10)}$$

Recall that $\nabla\phi_r$, $\nabla\phi_z$, and $\bar{A}$ are for the differential current element at $z' = 0$. One can see from Eq. A3.10 that $d\bar{E}$ has the radial (r) and vertical (z) components and that $\nabla\phi$ contributes to both the r- and z-components of $d\bar{E}$, while $\partial\bar{A}/\partial t$ only to the z-component. The two components of $d\bar{E}$ can be expressed as follows:

$$dE_r = \frac{dz'}{4\pi\varepsilon_0}\left[\frac{3rz}{R^5}\int_0^t I(\tau - R/c)d\tau + \frac{3rz}{cR^4}I(t - R/c) + \frac{rz}{c^2R^3}\frac{\partial I(t - R/c)}{\partial t}\right] \qquad \text{(A3.11)}$$

$$dE_z = \frac{dz'}{4\pi\varepsilon_0}\left[\frac{2z^2 - r^2}{R^5}\int_0^t I(\tau - R/c)d\tau + \frac{2z^2 - r^2}{cR^4}I(t - R/c) - \frac{r^2}{c^2R^3}\frac{\partial I(t - R/c)}{\partial t}\right] \qquad \text{(A3.12)}$$

In the dE_z equation, the geometrical factors in the three terms were obtained as follows:

$$\frac{3z^2}{R^5} - \frac{1}{R^3} = \frac{3z^2 - R^2}{R^5} = \frac{3z^2 - z^2 - r^2}{R^5} = \frac{2z^2 - r^2}{R^5} \qquad \text{1st term (electrostatic)}$$

$$\frac{3z^2}{cR^4} - \frac{1}{cR^2} = \frac{3z^2 - R^2}{cR^4} = \frac{3z^2 - z^2 - r^2}{cR^4} = \frac{2z^2 - r^2}{cR^4} \qquad \text{2nd term (induction)}$$

$$\frac{z^2}{c^2R^3} - \frac{1}{c^2R} = \frac{z^2 - R^2}{c^2R^3} = \frac{z^2 - z^2 - r^2}{c^2R^3} = -\frac{r^2}{c^2R^3} \qquad \text{3rd term (radiation)}$$

A3.2 Elevated differential current element ($z' > 0$) and its image

Now we assume that the lower half-space ($z < 0$) is perfectly conducting ground and that the differential current element is elevated to height $z' > 0$. The field point remains at the same position as in Section A3.1. The presence of perfectly conducting ground can be accounted for by using the image theory; that is, by placing an image current element, having the same magnitude and the same direction as the real one, at distance z' below the ground surface. The vectorial sum of field contributions from the real and image current elements at field point P at $z > 0$ in this configuration (see Fig. A3.1b) is identical to the field at point P in the original configuration (a single current element above the ground plane).

In order to make the equations for $d\bar{B}$ and $d\bar{E}$ derived in Section A3.1 applicable to the real and image current elements located at z' and $-z'$, respectively, the following changes are to be made.

For the real current element we simply replace z with $(z - z')$ in the electric field equations:

$$dE_r = \frac{dz'}{4\pi\varepsilon_0}\left[\frac{3r(z-z')}{R^5}\int_0^t I(z',\ \tau - R/c)d\tau + \frac{3r(z-z')}{cR^4}I(z',\ t - R/c) + \frac{r(z-z')}{c^2R^3}\frac{\partial I(z',\ t-R/c)}{\partial t}\right] \quad \text{(A3.13)}$$

$$dE_z = \frac{dz'}{4\pi\varepsilon_0}\left[\frac{2(z-z')^2 - r^2}{R^5}\int_0^t I(z',\ \tau - R/c)d\tau + \frac{2(z-z')^2 - r^2}{cR^4}I(z',\ t - R/c) - \frac{r^2}{c^2R^3}\frac{\partial I(z',\ t-R/c)}{\partial t}\right] \quad \text{(A3.14)}$$

where $R = \sqrt{r^2 + (z-z')^2}$. The equation for the ϕ-component of magnetic field (B_ϕ) is similar to Eq. A3.4, the only differences being the change in the argument of current function from $(t - R/c)$, where $z' = 0$ is implied, to $(z', t - R/c)$ and different expression for R (see above):

$$dB_\phi = \frac{\mu_0 dz'}{4\pi}\left[\frac{r}{R^3}I(z',\ t - R/c) + \frac{r}{cR^2}\frac{\partial I(z',\ t-R/c)}{\partial t}\right] \quad \text{(A3.15)}$$

Note that the two terms in the brackets in Eq. A3.15 are transposed relative to Eq. A3.4 in order to make the magnetic field equation consistent with the traditional formulation in which the $\partial I/\partial t$ term follows the I term.

Equations for the image current element can be obtained from the equations for the real one (Eqs. A3.13–A3.15 above) by replacing $(z - z')$ with $(z + z')$ and R with $R_I = \sqrt{r^2 + (z+z')^2}$.

A3.3 Elevated differential current element above ground and its image; field point on the ground surface

When $z = 0$ (point P on the ground surface; see Fig. A3.1c), $R_I = R$ and, hence, contributions from the real and image sources are equal to each other. Thus, the effect of perfectly conducting ground plane on the magnetic field on that plane is to double the contribution from the real current element.

Similarly, the contributions from the real and image current elements to E_z are equal, causing the field doubling effect, while the contributions to E_r are equal in magnitude and

opposite in sign. Hence, the radial component of electric field on perfectly conducting ground is zero, as required by the boundary condition on the tangential component of electric field on the dielectric/conductor interface; only normal component can exist on the surface of a perfect conductor.

The total electric and magnetic fields at the ground surface (z = 0) due to the elevated differential current element and its image are given by

$$dE_z(t) = \frac{dz'}{2\pi\varepsilon_0}\left[\frac{2z'^2 - r^2}{R^5}\int_0^t I(z',\ \tau - R/c)d\tau + \frac{2z'^2 - r^2}{cR^4}I(z',\ t - R/c) - \frac{r^2}{c^2R^3}\frac{\partial I(z',\ t - R/c)}{\partial t}\right] \quad \text{(A3.16)}$$

Make this bracket large.

$$dB_\phi(t) = \frac{\mu_0 dz'}{2\pi}\left[\frac{r}{R^3}I(z',\ t - R/c) + \frac{r}{cR^2}\frac{\partial I(z',\ t - R/c)}{\partial t}\right] \quad \text{(A3.17)}$$

Equations A3.16 and A3.17 are applicable to an electrically short vertical dipole above ground, such as the compact intracloud discharge (CID; see Appendix 4). The three terms in Eq. A3.16 are named electrostatic, induction, and radiation, and in Eq. A3.17 the two terms are magnetostatic and radiation.

A3.4 Vertical lightning channel above ground; field point on the ground surface

This configuration is usually applied to the return-stroke process in which a current wave propagates from the ground level up along the channel.

Integrating Eq. A3.16 over the radiating channel length H(t) we get

$$E_z(t) = \frac{1}{2\pi\varepsilon_0}\left[\int_0^{H(t)}\frac{2z'^2 - r^2}{R^5}\int_0^t I(z',\ \tau - R/c)d\tau dz' + \int_0^{H(t)}\frac{2z'^2 - r^2}{cR^4}I(z',\ t - R/c)dz' - \int_0^{H(t)}\frac{r^2}{c^2R^3}\frac{\partial I(z',\ t - R/c)}{\partial t}dz'\right] \quad \text{(A3.18)}$$

Make these brackets large.

Alternatively, we can write

$$E_z(t) = \frac{1}{2\pi\varepsilon_0}\left[\int_0^{H(t)}\frac{(2 - 3\sin^2\theta)}{R^3}\int_0^t I(z',\ \tau - R/c)d\tau dz' + \int_0^{H(t)}\frac{(2 - 3\sin^2\theta)}{cR^2}I(z',\ t - R/c)dz' - \int_0^{H(t)}\frac{\sin^2\theta}{c^2R}\frac{\partial I(z',\ t - R/c)}{\partial t}dz'\right] \quad \text{(A3.19)}$$

2013

- Lightning parameters for engineering applications, Electra, No. 269, August 2013, 58–65, V. A. Rakov, A. Borghetti, C. Bouquegneau, W. A. Chisholm, V. Cooray, K. Cummins, G. Diendorfer, F. Heidler, A. Hussein, M. Ishii, C. A. Nucci, A. Piantini, O. Pinto, Jr., X. Qie, F. Rachidi, M. M. F. Saba, T. Shindo, W. Schulz, R. Thottappillil, S. Visacro, and W. Zischank
- Rocket-and-Wire Triggered Lightning in 2012 Tropical storm debby in the absence of natural lightning, J. Geophys. Res., Atmos, published December 3, 2013, J. T. Pilkey, M. A. Uman, J. D. Hill, T. Ngin, W. R. Gamerota, D. M. Jordan, W. Rison, P. R. Krehbiel, H. E. Edens, M. I. Biggerstaff, and P. Hyland, doi:10.1002/2013JD020501
- Electromagnetic methods of lightning detection, surveys in geophysics (Springer), Vol. 34, No. 6, November 2013, 731–53, V. A. Rakov, doi: 10.1007/s10712–013–9251–1
- The angular distribution of energetic electron and X-ray emissions from triggered lightning leaders," J. Geophys. Res. Atmos., Vol. 118, 11,712–26, October 23, 2013, M. M. Schaal, J. R. Dwyer, H. K. Rassoul, J. D. Hill, D. M. Jordan, and M. A. Uman, doi:10.1002/2013JD019619
- Measurement and analysis of ground-level electric fields and wire-base current During the rocket-and-wire lightning triggering process, J. Geophys. Res. Atmos., Vol. 118, 10,041–55, published September 10, 2013, T. Ngin, M. A. Uman, J. D. Hill, J. Pilkey, W. R. Gamerota, D. M. Jordan, and R. C. Olsen, doi:10.1002/jgrd.50774
- Initiation processes of return strokes in rocket-triggered lightning, J. Geophysical Research: Atmospheres, J. Geophys. Res., Vol. 118, 9880–8, published September 6, 2013, D. Wang, N. Takagi, W. R. Gamerota, M. A. Uman, J. D. Hill, and D. M. Jordan, doi:10.1002/jgrd.50766
- The physics of lightning, surveys in geophysics (Springer), 2013, Vol. 34, No. 6, November 2013, 701–29, V. A. Rakov, doi: 10.1007/s10712–013–9230–6
- Correlated lightning mapping array and radar observations of the initial stage of three sequentially triggered Florida lightning discharges, J. Geophys. Res., Vol. 118, 8460–81, published August 15, 2013, J. D. Hill, J. Pilkey, M. A. Uman, D. M. Jordan, W. Rison, P. R. Krebhiel, M. I. Biggerstaff, P. Hyland, and R. Blakeslee, doi:10.1002/jgrd.50660
- Review of recent developments in lightning channel corona sheath research, Atmos. Res., Vols. 129–30, 2013, 117–22, G. Maslowski and V. A. Rakov, doi:10.1016/j.atmosres.2012.05.028
- An "Anomalous" triggered lightning flash in Florida, J. Geophys. Res., Vol. 118, 3402–14, published April 25, 2013, W. R. Gamerota, M. A. Uman, J. D. Hill, J. Pilkey, T. Ngin, D. M. Jordan, and C. T. Mata, doi: 10.1002/jgrd.50261

2012

- Geometrical and electrical characteristics of the initial stage in Florida triggered lightning, Geophys. Res. Lett., Vol. 39, L09807, 2012, J. D. Hill, J. Pilkey, M. A. Uman, D. M. Jordan, W. Rison, and P. R. Krehbiel, doi:10.1029/2012GL051932

Lu, W., Chen, L., Ma, Y., Rakov, V. A., Gao, Y., Zhang, Y., Yin, Q. and Zhang, Y. (2013). Lightning attachment process involving connection of downward negative leader to the lateral surface of upward connecting leader. *Geophys. Res. Lett.*, 40: 5531–35, doi:10.1002/2013GL058060

Lü, F., Zhu, B., Zhou, H., Rakov, V. A., Xu, W. and Qin, Z. (2013). Observations of compact intracloud lightning discharges in northernmost region (51° N) of China. *J. Geophys. Res. Atmos.*, 118: 4458–65, doi:10.1002/jgrd.50295.

MacGorman, D. R., Maier, M. W. and Rust, W. D. (1984). *Lightning strike density for the contiguous United States from thunderstorm duration records,* NUREG/CR-3759, Office of Nuclear Regulatory Research, U.S. Nuclear Regulatory Commission, 44 p., Washington, DC.

MacGorman, D. R. and Rust, W. D. (1998). *The Electrical Nature of Thunderstorms*, 422 p., New York: Oxford University Press.

Mach, D. M., MacGorman, D. R., Rust, W. D. and Arnold, R. T. (1986), Site errors and detection efficiency in a magnetic direction-finder network for locating lightning strikes to ground. *J. Atmos. Ocean. Tech.*, 3: 67–74.

Malan, D. J. (1952). Les déchargesdansl'airet la charge inférieure positive d'un nuageorageuse. *Ann. Geophys.*, 8: 385–401.

Mallick, S. et al. (2014a). Performance characteristics of the NLDN for return strokes and pulses superimposed on steady currents, based on rocket-triggered lightning data acquired in Florida in 2004–2012. *J. Geophys. Res. Atmos.*, 119: 3825–56, doi:10.1002/2013JD021401.

Mallick, S., Rakov, V. A., Hill, J. D., Ngin, T., Gamerota, W. R., Pilkey, J. T., Jordan, D. M., Uman, M.A., Heckman, S., Sloop, C. D. and Liu, C. (2015). Performance characteristics of the ENTLN evaluated using rocket-triggered lightning data. *Electric Power Systems Research*, 118: 15–28.

Mallick, S., Rakov, V. A., Ngin, T., Gamerota, W. R., Pilkey, J. T., Hill, J. D., Uman, M. A., Jordan, D. M., Cramer, J. A. and Nag, A. (2014a). An Update on the Performance Characteristics of the NLDN, *2014 ILDC/ILMC*, Tucson, Arizona, USA.

Mallick, S., Rakov, V. A., Ngin, T., Gamerota, W. R., Pilkey, J. T., Hill, J. D., Uman, M. A., Jordan, D. M., Nag, A. and Said, R. K. (2014b). Evaluation of the GLD360 performance characteristics using rocket-and-wire triggered lightning data. *Geophys. Res. Lett.*, 41: 3636–42, doi:10.1002/2014GL059920.

Mallick, S., Rakov, V. A., Ngin, T., Gamerota, W. R., Pilkey, J. T., Hill, J. D., Uman, M. A., Jordan, D. M., Hutchins, M. L. and Holzworth, R. H. (2014). Evaluation of the WWLLN Performance Characteristics Using Rocket-triggered Lightning Data, *2014 GROUND/LPE*, Manaus, Brazil.

Mallick, S., Rakov, V. A., Tsalikis, D., Nag, A., Biagi, C., Hill, D., Jordan, D. M., Uman, M. A. and Cramer, J. A. (2014). On remote measurements of lightning return stroke peak currents. *Atmos. Res.*, 135–136: 306–13.

Marshall, R. A., da Silva, C. L. and Pasko, V. P. (2015). Elve doublets and compact intracloud discharges. *Geophys. Res. Lett.*, 42: 6112–19, doi:10.1002/2015GL064862.

Marshall, T. C. and Rust, W. D. (1991). Electric field soundings through thunderstorms. *J. Geophys. Res.*, 96: 22,297–306.